Catalysis Letters
https://doi.org/10.1007/s10562-019-02927-z

Yttrium Oxide Supported La_2O_3 Nanomaterials for Catalytic Oxidative Cracking of *n*-Propane to Olefins

Fawaz S. Al-Sultan[1] · Sulaiman N. Basahel[1] · Katabathini Narasimharao[1]

Received: 10 March 2019 / Accepted: 7 August 2019

Abstract

La_2O_3 nanorods were prepared by simple hydrothermal synthesis method. Yttrium oxide (1, 3, 5 and 7 wt%) supported La_2O_3 and SO_4^{2-} incorporated La_2O_3 nanorods were prepared impregnation method and used as catalysts in oxidative cracking of *n*-propane. The pure La_2O_3 nanorods exhibited 15% *n*-propane conversion with 22% olefins (ethane and propene) selectivity. Considerable improvement in *n*-propane conversion was observed in case of 3 wt% yttrium oxide supported on La_2O_3 nanorods (25% conversion of *n*-propane and 36% selectivity to olefins) at reaction temperature of 550 °C. Interestingly, 5 wt% yttrium oxide supported 10 wt% SO_4^{2-}/La_2O_3 nanorod sample exhibited superior performance in *n*-propane conversion (42%) and olefins selectivity (54%). The yttrium oxide loading and sulfation of La_2O_3 nanorods influenced the catalytic activity. The characterization of synthesized nanomaterials was performed using elemental analysis, XRD, FT-IR, N_2-physisorption, SEM, XPS and H_2-TPR techniques. The obtained results indicated that yttrium oxide was highly dispersed over the La_2O_3 nanorods because of strong interaction between the two rare earth metal oxides. Additionally, deposition of yttrium oxide to sulfated La_2O_3 nanorods increased the surface area and the amount of Lewis acid sites (for the activation of *n*-propane) on La_2O_3 nanorods. Yttrium oxide supported sulfated La_2O_3 catalyst showed no deactivation during the 24 h of reaction and without coke formation.

Graphic Abstract

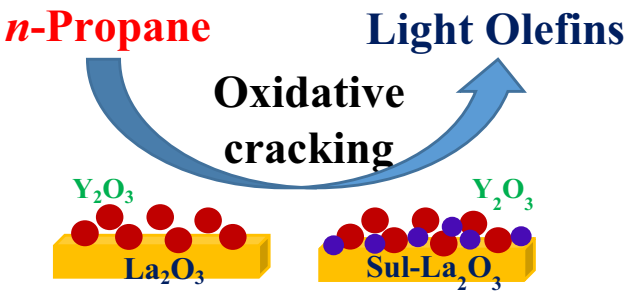

Keywords Yttrium oxide · La_2O_3 nanorods · Sulfated La_2O_3 · *n*-Propane · Catalytic oxidative cracking

1 Introduction

Light olefins such as ethene and propene are important raw materials in syntheses of alcohols, plastics, detergents and fuels [1]. The demand for the light olefins is anticipated to surge considerably in coming years and the light olefins are conventionally manufactured from natural gas and crude oil by steam cracking, fluid-catalytic-cracking, and catalytic dehydrogenation processes [2]. Though, listed

Electronic supplementary material The online version of this article (https://doi.org/10.1007/s10562-019-02927-z) contains supplementary material, which is available to authorized users.

✉ Katabathini Narasimharao
nkatabathini@kau.edu.sa

[1] Surface Chemistry and Catalytic Studies (SCCS) Group, Department of Chemistry, Faculty of Science, King Abdulaziz University, P. O. Box 80203, Jeddah 21589, Kingdom of Saudi Arabia

Published online: 17 August 2019

processes are extensively studied, these processes are suffering from drawbacks that the manufacturing of olefins is not up to the market demand and also high energy requirement, formation of coke which is responsible for catalyst deactivation [3]. The catalytic oxidative cracking has become an alternative to steam cracking process as it is possible to make the olefins production process less energy consuming by adding oxygen in the reactants stream in presence of catalyst which facilitates cracking of alkanes at low reaction temperatures [4]. Fabrication of an effective catalyst technology is essential, which could offer high alkane conversion and selectivity to olefins in presence of oxygen without excessive oxidation of alkane and olefins [5, 6]. Although, many research reports were existed in the literature on fabrication of efficient catalyst for the oxidative dehydrogenation of hydrocarbons, very few studies were existed pertaining to catalytic oxidative cracking of hydrocarbons [7]. Researchers utilized different types of catalysts; acidic catalysts (dealuminated H-ZSM-5, Cu loaded H-ZSM-5), basic catalysts (Ca-Sr-Al and W-K-Al mixed oxides) and transition metal oxide catalysts (Cr–Al and V-oxides) [8].

The rare earth metals could be categorized as light or heavy (as per their electronic configuration) and possessed different chemical, electrical and catalytic properties [9]. These are key components in fluid cracking catalyst and the results indicated that rare earth metal exchanged zeolites are more active than the traditional transition metal oxide catalysts in fluid cracking process [10, 11]. Yoshimura et al. [12] indicated alkali metal doped La_2O_3 catalysts offers high selectivities to light alkenes in oxidative cracking of n-butane process. Nakamura et al. [13] synthesized Li supported rare earth oxides (La_2O_3, Y_2O_3, Sm_2O_3 and Gd_2O_3) for oxidative cracking of *n*-butane and the authors observed that Li supported Y_2O_3 offered superior performance. Wakui et al. [14] used La modified HZSM-5 materials for *n*-butane cracking and authors reported that these catalysts exhibited mild activity. Sa et al. [15] utilized gold supported La_2O_3 and sulfated La_2O_3 catalysts for oxidative cracking of *n*-butane.

It is known that impregnation of sulfate anions over metal oxides provides robust solid acid catalysts which possesses strong Brönsted acid sites to enhance the rate of acid catalyzed reactions [16, 17]. In our previous studies, gold supported sulfated $CeZrO_2$ and La_2O_3 were identified as effective catalysts for oxidative cracking of *n*-propane [18, 19]. In this contribution, yttrium (heavy rare earth metal) oxide supported over lanthanum (light rare earth metal) oxide and sulfated lanthanum oxide nanomaterials were synthesized and used as catalysts for oxidative cracking of *n*-propane for the first time. The physico-chemical properties of yttrium oxide supported over La_2O_3 nanorods were investigated using XRD, FT-IR, SEM, N_2-physisorption, XPS, acidity measurements and H_2-TPR methods. An effort was made to relate the oxidative catalytic cracking performance with their physico-chemical characteristics.

2 Experimental

2.1 Synthesis of Catalysts

2.1.1 Bulk La_2O_3 and Sulfated La_2O_3 Nanorods

Hydrothermal synthesis method was utilized to synthesize bare La_2O_3 nanorods. In a typical synthesis, 2.0 g of lanthanum nitrate was added to 30 mL of double distilled water, to this 18 g of KOH was added and the total contents were moved into a Teflon lined stainless steel autoclave and it was placed in an electric oven and the temperature of the oven was raised to 200 °C and kept it for 48 h. After the hydrothermal treatment, the autoclave was brought to temperature of 25 °C and the obtained solid product was collected and washed by using distilled water and with dil. HCl to eliminate the excess potassium hydroxide. The washed cake was then calcined at 600 °C for 6 h in air to obtain nanorods of La_2O_3. Sulfation of La_2O_3 nanorods was performed using diluted H_2SO_4 by simple wet chemical impregnation. A calculated quantity of La_2O_3 nanorods sample was immersed in 1.0 M H_2SO_4 solution (for 1.0 g of La_2O_3-NR, 15 mL of 0.1 M H_2SO_4). The resulted H_2SO_4–La_2O_3 mixture was dried at 100 °C for 12 h and the obtained material was calcined at 600 °C for 4 h to acquire the sulfated La_2O_3-NR.

2.1.2 Yttrium Oxide Deposited La_2O_3 and Sulfated La_2O_3

Yttrium oxide supported La_2O_3 and sulfated La_2O_3 nanomaterials were obtained using impregnation technique. Calculated quantity of La_2O_3 or sulfated La_2O_3 nanorods sample was immersed in an aqueous solution of yttrium nitrate (BDH chemicals, UK) corresponding to 1, 3, 5 and 7 wt% of yttrium oxide. The total contents were stirred for 2 h and the resultant material was then dried at 100 °C for 12 h. The dried materials were calcined at 600 °C for 4 h in an electric furnace in presence of air.

2.2 Characterization of Synthesized Materials

The elemental composition of the synthesized materials was determined by using ICP-AES, Optima 7300DV (Perkin-Elmer) instrument. The sulfur content of the catalysts was determined by CHNS elemental analysis using Perkin-Elmer 2400 instrument. The XRD patterns of the powders were collected by using PANalytical XpertPro diffractometer. The crystallite size of obtained materials was determined by applying the Scherer Eq. (1).

$$D = B\,\lambda/\beta_{1/2}\cos\theta \tag{1}$$

where 'D' is the average crystallite size of the phase under investigation, 'B' is the Scherrer constant (0.89), 'λ' is wavelength of the X-ray beam used (1.5405 Å), '$\beta_{1/2}$' is the full width at half maximum (FWHM) of the diffraction peak and 'θ' is the diffraction angle. The SEM analysis of the samples was carried out using JEOL Model JSM-6390LV microscope. The FTIR spectra of calcined materials were obtained using Bruker vertex 70 FTIR spectrometer. The acidic character of the samples was investigated by pyridine adsorption measurements using FTIR spectroscopy; the analysis was performed over calculated amount of catalyst, which was treated at 100 °C under vacuum for 5 h. Then, the sample was treated with pyridine vapor and finally heated at 100 °C under vacuum for 30 min to remove physically adsorbed pyridine. FT-IR spectra were collected at room temperature [18]. XPS spectra of the materials were collected by using Kratos Axis Nova spectrometer. The textural properties of the samples were obtained by carrying out the N_2-physisorption experiments over Quantachrome ASiQ adsorption system. The reducibility of the samples was investigated by using H_2-temperature-programmed reduction using Quantachrome CHEMBET-3000 system.

2.3 Catalytic Oxidative Cracking of *n*-Propane

Catalytic oxidative cracking of *n*-propane tests were performed using a fixed bed quartz reactor. The reactor was loaded with weighed catalyst pellets (200 mg), which were diluted with unreactive quartz particles. The reactant gas mixture, which contained *n*-propane (20 mL min^{-1}), 20% oxygen—80% argon (100 mL min^{-1}) and argon (40 mL min^{-1}) was used to perform the catalytic tests. Different reaction temperatures were used to investigate the effect of reaction temperature on the catalyst performance. The composition of product gas mixture was continuously analyzed with the help of Agilent 6890 A gas chromatograph equipped with flame ionization and thermal conductivity detectors.

3 Results and Discussion

3.1 Physico-Chemical Properties of Yttrium Supported La_2O_3 Nanorod Samples

The powder XRD patterns of the samples are shown in Fig. S1. Appearance of prominent X-ray reflections in all the samples indicating that the synthesized samples are polycrystalline in nature. The synthesized La_2O_3-NR sample exhibited major reflections corresponding to the $La(OH)_3$ phase [JCPDS: 36-1481] along with major reflections due to hexagonal La_2O_3 phase [JCPDS: 05-0602]. Although, the samples were calcined at 600 °C, the samples showed $La(OH)_3$ as a main phase because of the hygroscopic nature of La_2O_3 and it was previously observed that $La(OH)_3$ generates from La_2O_3 under atmospheric conditions [20]. The yttrium oxide supported La_2O_3-NR samples exhibited additional reflections around 24°, 30° and 32°, which could be due to the presence of cubic phase of Y_2O_3 [JCPDS: 895591]. Presence of the reflections due to Y_2O_3 in all the samples indicating the formation of Y_2O_3 crystals in these samples. Sulfated La_2O_3-NR sample and yttrium oxide supported sulfated La_2O_3-NR samples exhibited La_2O_3 and Y_2O_3 phases and interestingly these samples have not exhibited presence of diffraction peaks corresponding to X-ray detectable lanthanum sulfate. A similar results were observed in case of sulfated microcrystalline La_2O_3 catalysts. However, there is a clearly possibility for the formation of amorphous lanthanum sulfate species, as major reflections due to $La(OH)_3$ phase were disappeared in case of sulfated sample. The crystallite size of the materials was determined from the XRD patterns using Scherer equation. The crystallite size of La_2O_3 phase for sulfated La_2O_3-NR and bare La_2O_3-NR samples was observed as 23 nm and 48 nm respectively. The crystal size of the sulfated La_2O_3-NR sample is much smaller than that of the bulk La_2O_3-NR.

FT-IR spectra for yttrium oxide supported La_2O_3 and sulfated La_2O_3 nanorods are shown in Fig. S2. The La_2O_3-NR and yttrium oxide supported La_2O_3-NR samples exhibited major band at 695 cm^{-1} which could be assigned to La–O bond [21] The minor bands appeared at 860 cm^{-1}, 1370 cm^{-1} and 1475 cm^{-1} could be attributed to the stretching vibrations of C=O functional groups of $[CO_3]^{2-}$ ions presented over the surface of the $La(OH)_3$ [22]. FT-IR spectra of yttrium oxide supported La_2O_3-NR samples are very similar as La_2O_3-NR sample except the intensity of La–O band was decreased considerably and also a new band appears at 563 cm^{-1}, which could be attributed to Y–O stretching vibration and the formation of Y_2O_3 [23]. Sulfated La_2O_3-NR and yttrium supported sulfated La_2O_3-NR samples showed additional bands at 1065 cm^{-1}, 1120 cm^{-1} and 1180 cm^{-1}, which could be attributed to the IR bands due to (O-SO) and (O-SO_3) functional moieties [24]. These results clearly indicating that the sulphated samples possessed the metal oxide-sulfate interactive species and these results confirm the efficiency of sulfation procedure steps. The bulk elemental analysis of the samples was determined by ICP-AES and CHNS techniques and the results are presented in Table 1. The bulk sulfur present in sulfated La_2O_3 sample was 1.15 wt% and a slight reduction of sulfur content was observed with yttrium oxide deposition. The morphology of synthesized samples was studied by SEM analysis. Figure 1 shows SEM images of representative samples. The SEM image of La_2O_3-NR, 3Y-La-NR and 7Y-La-NR samples clearly shows the presence of nanorods with several micrometers in length and typical widths of 40–50 nm. Sulfation

Table 1 Textural properties of yttrium oxide supported La_2O_3 and sulfated La_2O_3 nanorods

Sample	Bulk elemental analysis (wt%)			Textural properties		
	La	Y	S	Surface area (m^2g^{-1})	Pore volume (ccg^{-1})	Pore diameter (nm)
La_2O_3-NR	85.2	–	–	59	0.142	15.4
1Y-La-NR	84.1	0.9	–	47	0.140	14.5
3Y-La-NR	81.2	2.8	–	44	0.136	14.5
5Y-La-NR	79.7	4.8	–	42	0.131	14.4
7Y-La-NR	78.3	6.9	–	39	0.127	14.4
Sul-La_2O_3-NR	83.6	–	1.15	71	0.153	14.9
1Y-Sul-La-NR	83.0	0.8	1.02	62	0.147	14.6
3Y-Sul-La-NR	81.5	2.7	0.88	59	0.142	14.4
5Y-Sul-La-NR	79.0	4.5	0.77	48	0.140	14.3
7Y-Sul-La-NR	77.2	6.5	0.72	45	0.137	14.2

of La_2O_3-NR has altered the morphology of the samples, breaking up of long nanorods morphologies is witnessed. The breaking of long nanorods into small and broad rod like structures were formed, as they can be seen in Fig. 1.

The samples with high yttrium oxide loading shows the cumulative nature of secondary particles, which are made up of agglomeration of Y_2O_3 particles. Presence of non-uniform structures could result a wide particle size distribution in samples with high yttrium oxide content and sulfated La_2O_3-NR samples. Fig. S3 represents DR UV–Vis spectra for yttrium oxide supported La_2O_3 and sulfated La_2O_3 nanorods. As shown in the figure, distinctive absorption La_2O_3 edge could be witnessed in the spectra of yttrium oxide supported La_2O_3 and sulfated La_2O_3-NR samples. The La_2O_3-NR sample showed major absorption band around 250 nm. Impregnation of yttrium oxide over the La_2O_3-NR sample resulted slight shift in band position to 255 nm and also an increase in the intensity of absorption band. The shift in the absorption could be attributed to the quantum size effect; This can be correlated with results obtained in the SEM images that the long nanorods were broke into smaller size nanorods, which should have increased the surface to volume ratio, thus increasing the absorbing capability of the samples after sulfation and yttrium oxide impregnation. It was previously reported that UV–Vis spectra of bulk Y_2O_3 nanoparticles exhibits two absorption bands at 250 nm and 300 nm and the prior one was attributed to band gap of Y_2O_3 and the later one could be attributed to the surface defect states [25]. It can be observed the appearance of a new weak absorption band at 300 nm in case of yttrium impregnated La_2O_3-NR and sulfated La_2O_3-NR samples.

To determine the textural properties of synthesized samples, N_2-physical adsorption experiments were performed. The N_2 adsorption–desorption isotherms of synthesized materials are presented in Fig. S4A. It is clear that all synthesized samples exhibited typical type IV adsorption isotherms with H3 hysteresis loops (IUPAC classification) and also the adsorption isotherms showed a sharp inflection in P/P° range of 0.8–1.0, indicating that the synthesized samples possessed meso pore structure, which could have raised due to the inter void spaces of nanorods. The pore size distribution patterns of the samples (Fig. S4B) were obtained from the desorption branch of the isotherms. The specific surface area, pore diameter and pore volume values for the investigated samples are presented in Table 1. It can be observed that the surface area, pore size and pore volume are steadily declined after yttrium oxide impregnation over La_2O_3-NR sample. However, it is clear that the decrease of the pore volume and pore size is small after deposition of yttrium oxide; therefore, it is possible to argue that most of the Y_2O_3 was located over the surface of La_2O_3-NR. In contrast, sulfation procedure resulted increased the surface area of La_2O_3-NR sample, probably due to the formation of lower size La_2O_3 nanorods and also amorphous interactive phase.

The surface composition and electronic states of different species presented in the synthesized samples were measured using XPS analysis (Fig. 2). It is known that La *3d* core spectrum split into $3d_{5/2}$ and $3d_{3/2}$ components due to a spin–orbit interaction. The calcined La_2O_3 sample exhibited XPS peaks at 835.8 eV & 839.3 eV and 852.6 eV & 856.3 eV corresponding to La $3d_{5/2}$ and La $3d_{3/2}$ states respectively (Fig. S5). Additionally, each line split into main and satellite peaks corresponding to $3d^0\ 4f^0$ and $3d^0\ 4f^1L$ configuration respectively [26]. However, it was reported that the nature of satellite peak depends on the type of La compound [27]. For La based metallic compounds, the satellite peak is due to charge fluctuation from $4f^0$ state to $4f^1$ state, while in other La compounds such as oxides, halides and sulfides, it arises from an electron transfer from ligand to La *4f* state. It was previously observed that bulk La_2O_3 sample shows XPS peaks at 835.8 eV and 839.3 eV corresponding to La $3d_{5/2}$ states (La in +3 oxidation state) [26]. It

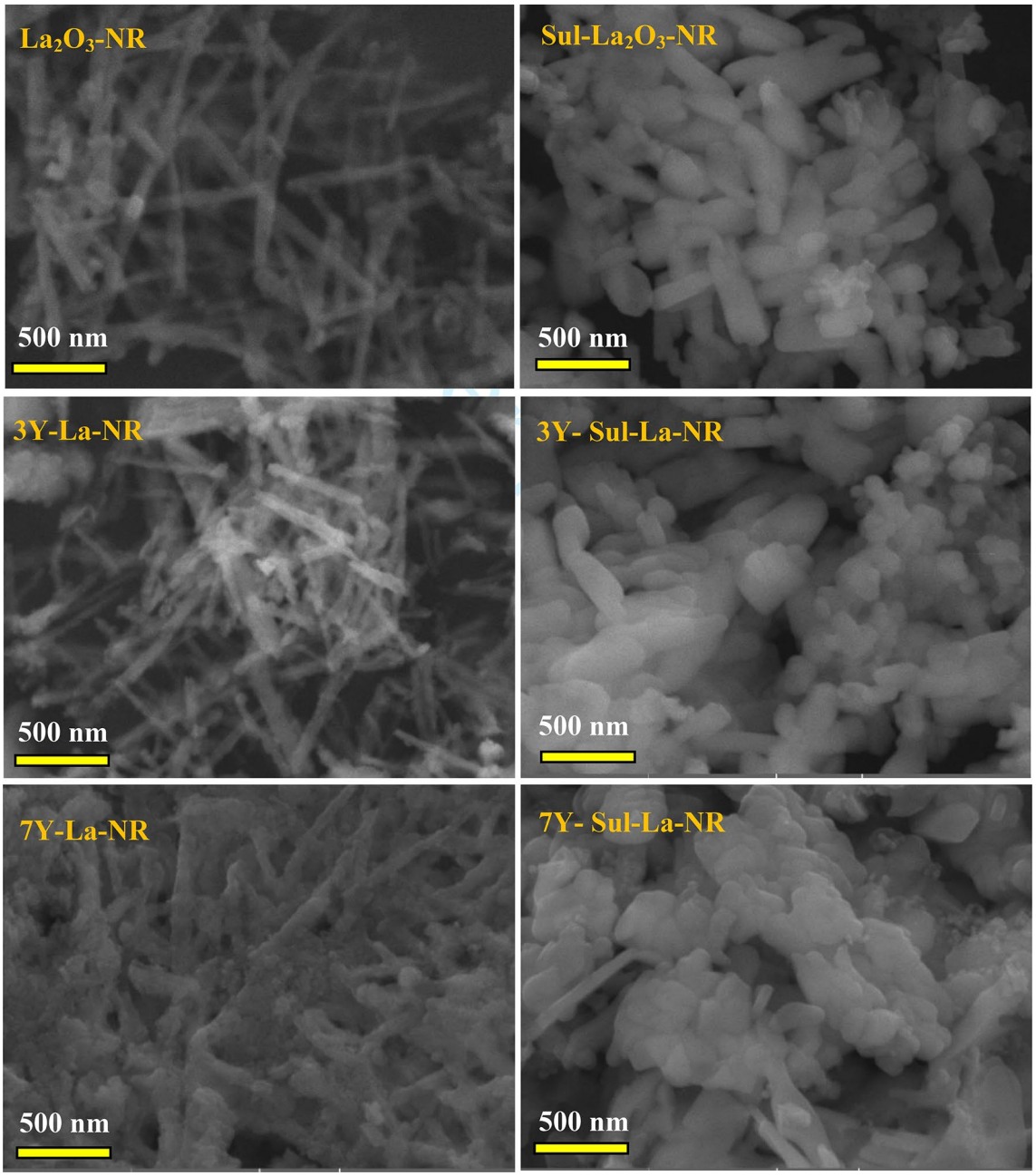

Fig. 1 SEM images of yttrium oxide supported La_2O_3 and sulfated La_2O_3 nanorods

was clearly observed that yttrium oxide supported La_2O_3-NR and sulfated La_2O_3-NR samples showed XP peaks at 834.6 and 838.1 eV corresponding to La $3d_{5/2}$ states. These observations indicating that the XP peak position for La *3d* states shifted to lower binding energy (BE) region after impregnation of sulfate and Y_2O_3 moieties. The shift in BE is mainly due to presence of interactive species (La-sulfate/Y_2O_3). The yttrium oxide supported La_2O_3-NR samples exhibited two Y *3d* peaks with BE of 157.3 eV and 159.3 eV correspond to stoichiometric Y_2O_3.

The Y *3d* peak position and shape are in good agreement with the XP peaks for Y_2O_3 [28]. Interestingly, the BE of two Y *3d* peaks are shifted to 157.5 eV and 159.5 eV in case of yttrium oxide supported sulfated La_2O_3-NR samples. The shift of BE of the Y *3d* doublet to higher binding energy due to interaction between Y and electronegative sulfate species [29]. To understand the interaction between the sulfur and rare earth oxides, the S *2p* photoelectron peak was deconvoluted into specific contributions in sulfated samples. It was reported that S *2p* peak could be deconvoluted into S $2p_{1/2}$

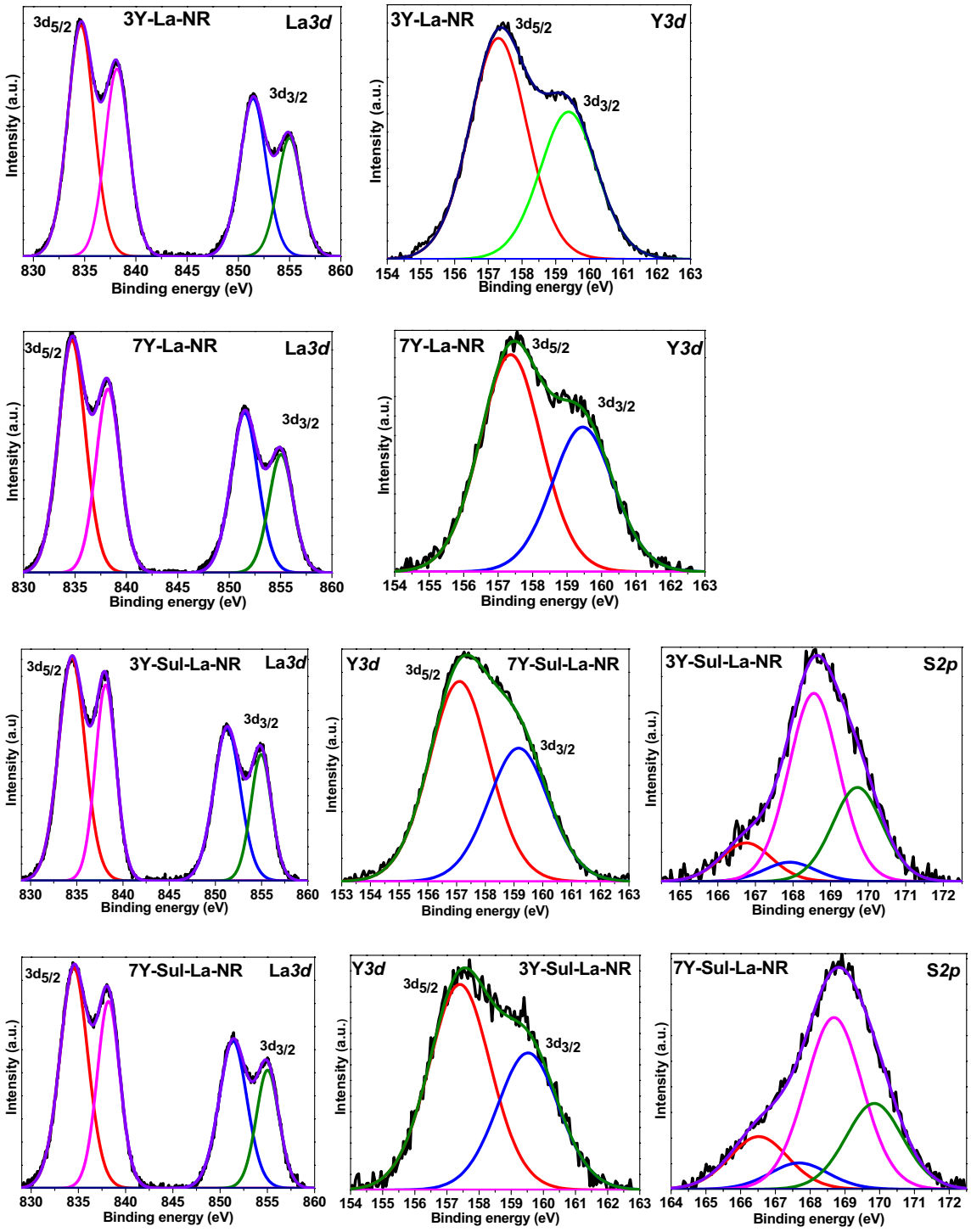

Fig. 2 X-ray photoelectron spectra of yttrium oxide supported La_2O_3 and sulfated La_2O_3 nanorods

and S $2p_{3/2}$ contributions due to spin–orbit splitting [30]. In case of sulfated La_2O_3, presence of two S $2p$ peaks at 168.8 eV and 170.0 eV were observed (Fig. S5).

It was also reported that the S $2p_{1/2}$ peak around 168.8 eV corresponding to the free S^{6+} species [31], and the peak around 170.0 eV could be attributed to metal-SO_4 species [32]. Presence of two sets of doublets (for both S $2p_{1/2}$ and S $2p_{3/2}$ contributions) could be observed in S $2p$ peak fittings for yttrium oxide deposited samples, therefore it is possible to argue that there are two types of surface sulfate species are existed in these samples as sulfated La_2O_3-NR sample. The contribution of peak at 170.0 eV is high in case

of 3Y-Sul-La-NR sample. The presence of less number of free sulfate groups in the yttrium oxide supported sulfated La_2O_3-NR samples explains the interaction of sulfate groups to surface of the metal sites.

Two major and one minor O*1s* XP peaks were observed for yttrium oxide supported La_2O_3-NR samples (Fig. S5). The peak at 528.8 eV BE (32.1%) could be due to the lattice oxygen in La_2O_3/Y_2O_3. The strongest peak (64.2%) at higher BE at 531.4 eV could be assigned to either adsorbed H_2O species [33], –OH groups or O^- surface atoms [34] Presence of high concentration of $H_2O/OH/O^-$ species indicating that these samples underwent high surface hydration. The appearance of the small XP peak in the O*1s* signal at 533.8 eV can be related to the surface interactive species such as La–O-Y species. Yttrium oxide impregnated sulfated La_2O_3-NR samples also showed three O*1s* species; the two XP peaks corresponding to lattice oxygen and $H_2O/OH/O^-$ species as similar to non-sulfated samples. However, the third peak shifted slightly to lower BE value (532.7 eV) and the intensity of the peak increased significantly, indicating that the concentration of interactive species is higher in the yttrium oxide supported sulfated La_2O_3 samples, revealing that the sulfation procedure is enhancing the generation of interactive species.

FTIR spectra of synthesized samples after pyridine adsorption were collected to study the nature of acidic sites (Fig S5). The obtained results indicated that synthesized samples exhibited peaks due to Brönsted (B) and Lewis acid sites (L) [18, 19]. The quantification of acid sites was performed using the FTIR spectra and the data is depicted in Table 2. Deposition of yttrium oxide resulted loss of Brönsted acid sites of the bare La_2O_3-NR sample. The results also revealed that impregnation of sulfate ions over La_2O_3-NR increased the number Brönsted acidic sites. It was previously revealed that Brönsted and Lewis acidic sites are useful for *n*-alkane activation. With the increase of yttrium oxide loading the total number of Lewis acid sites were increased and the number of Brönsted acid sites were diminished considerably, indicating that the deposition of yttrium oxide results decreases the acidic strength of the sulfated La_2O_3-NR samples.

Table 2 Acidity of the catalysts from pyridine adsorption measurements

Catalyst	Number of active sites		B/L ratio	Number of total sites
	Lewis (L)	Brönsted (B)		
La_2O_3-NR	10.2	4.3	0.421	14.5
1Y-La-NR	11.1	3.5	0.315	14.6
3Y-La-NR	12.5	3.0	0.240	15.5
5Y-La-NR	13.3	2.7	0.203	15.7
7Y-La-NR	14.2	2.0	0.140	16.2
Sul-La_2O_3-NR	10.7	10.1	0.943	20.8
1Y-Sul-La-NR	13.5	9.2	0.685	22.7
3Y-Sul-La-NR	17.1	7.0	0.409	24.1
5Y-Sul-La-NR	17.4	6.1	0.350	23.5
7Y-Sul-La-NR	17.5	4.7	0.268	22.2

H_2-temperature programmed reduction (H_2-TPR) analysis was used to study the reducibility of the yttrium oxide supported La_2O_3 and sulfated La_2O_3 nanorods and the patterns are shown in Fig. 3. The La_2O_3-NR sample exhibited a main peak at 650 °C and a minor peak at 740 °C. It is known that La_2O_3 is reducible at high temperatures and it is clear that La_2O_3 was reduced in two stages from bulk La_2O_3 to La metal. The La_2O_3-NR sample exhibited two TPR peaks after sulfation, however the temperature maximum of the TPR peaks was shifted to 615 and 670 °C respectively. This observation indicating that impregnation of sulfate groups enhanced the reducibility of La_2O_3.

The yttrium oxide impregnated samples showed a broad minor peak at 525 °C and another incomplete peak at about 800 °C. These new peaks show significant broadening and this phenomenon could be due to the random distribution of La and Y ions in the samples. Sasikala et al. [35] observed similar results in case of cerium-yttrium mixed

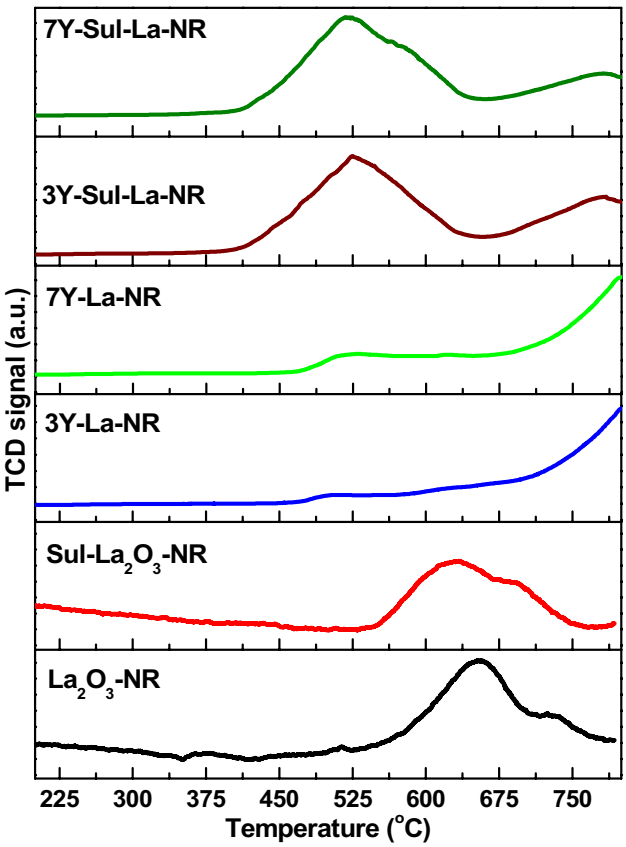

Fig. 3 H_2-TPR patterns of yttrium oxide supported La_2O_3 and sulfated La_2O_3 nanorods

oxide catalysts. The yttrium oxide impregnated sulfated La_2O_3-NR samples showed similar TPR peaks as yttrium oxide impregnated over La_2O_3-NR samples, however the intensity of the lower temperature reduction peak was significantly increased; probably due to existence of interaction between metal (La/Y) and sulfate ions. This observation indicating that promotion of yttrium oxide-La_2O_3 nanorods with sulfate ions lead to an increase in reducibility.

3.2 Oxidative Cracking Activity of Catalysts

Previously, we observed that micro crystalline La_2O_3 exhibited higher oxidative cracking activity than other bulk oxide supports tested [19]. Au et al. [36] indicated that surface O^- and O_2^{2-} species from basic and non-reducible La_2O_3 are responsible for its superior activity. It is well known that lowering the size of catalyst particles from micro to nano size could greatly enhance the catalytic activity. To study the role of the particle size, in this study nanosized La_2O_3 sample was prepared and investigated its ability in catalysing oxidative cracking of *n*-propane. The catalytic activity results of synthesized materials tested at different reaction temperature are presented in the Fig. 4.

Clearly, the bare La_2O_3-NR sample offered better performance compare to micro sized La_2O_3 (15.8% conversion and 18.4% selectivity to olefins at 600 °C) under identical reaction conditions [37]. Impregnation of 1 wt% yttrium oxide over La_2O_3-NR resulted slight improvement in the catalytic oxidative cracking activity. Increase of yttrium oxide loading to 3 wt% increased both conversion of *n*-propane and selectivity to olefins to 35% and 27.2% at 600 °C respectively [Fig. 4]. However, further increase of yttrium oxide loading to 5 and 7 wt% resulted decrease in n-propane conversion, indicating that yttrium oxide loading influences the oxidative cracking ability and 3 wt% appears to be optimum for the La_2O_3 nanorods support. Increase of reaction temperature from 450 to 650 °C resulted gradual increase in *n*-propane conversion for all investigated catalysts. A similar behavior was observed in our previous studies over $Ce_{0.5}Zr_{0.5}O_2$ and La_2O_3 based catalysts.

The selectivity to light olefins was also improved after impregnation of yttrium oxide loading over La_2O_3-NR support. It is well reported that C–H bond activation is the rate limiting stage in oxidative cracking of *n*-alkanes [18, 19]; existence of yttrium oxide on the surface of La_2O_3-NR is the reason for the improvement in catalyst performance in oxidative cracking process. There is a clear possibility for the existence of synergetic effect between La_2O_3-NR and yttrium oxide due to formation of interactive species. With increase of reaction temperature, the selectivity to olefins increased initially (from 450 to 550 °C), however further increase of reaction temperature resulted decrease in selectivity to olefins. It is known carbonization of olefins occurs at high reaction temperature [37].

Previously, it was also observed that sulfation of La_2O_3 resulted an enhancement in oxidative cracking activity. The previous results indicated that 10 wt% sulfate ions loading is optimum to obtain better oxidative cracking activity in case of gold supported La_2O_3 samples [19] and it is possibly due to the existence of La_2O_3-sulfate interactive species. Also, in this work, La_2O_3-NR sample was loaded with 10 wt% sulfate ions to take advantage of beneficial role of sulfate ions. Figure 5 represents the catalytic oxidative cracking activity of yttrium oxide supported sulfated La_2O_3-NR at different reaction temperatures. The results clearly indicated that sulfation of La_2O_3-NR increased the oxidative cracking ability of La_2O_3-NR support. Considerable alteration in catalytic activity was observed after impregnation of yttrium oxide on the surface of $10SO_4^{2-}/La_2O_3$-NR support. Both conversion of *n*-propane and selectivity to olefins were increased

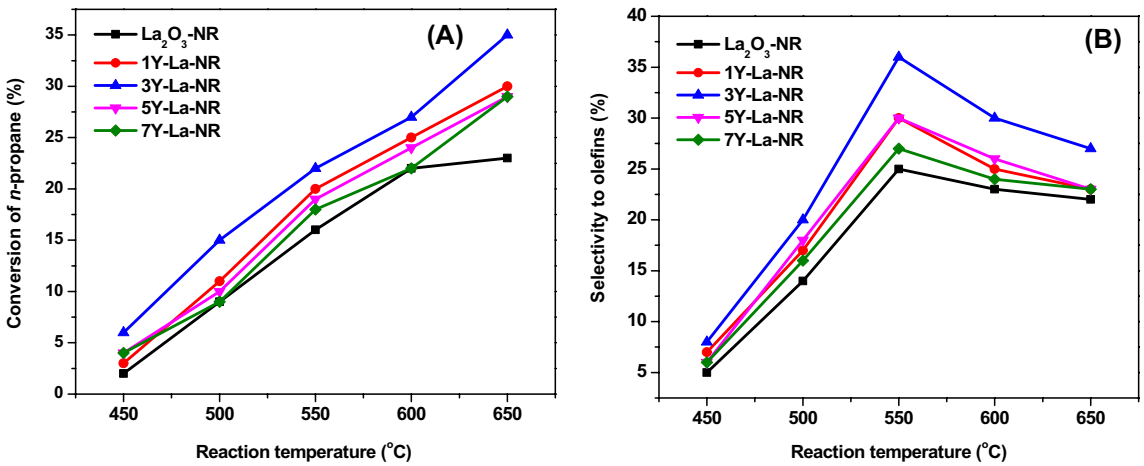

Fig. 4 Catalytic activity patterns of synthesized catalysts at different reaction temperatures

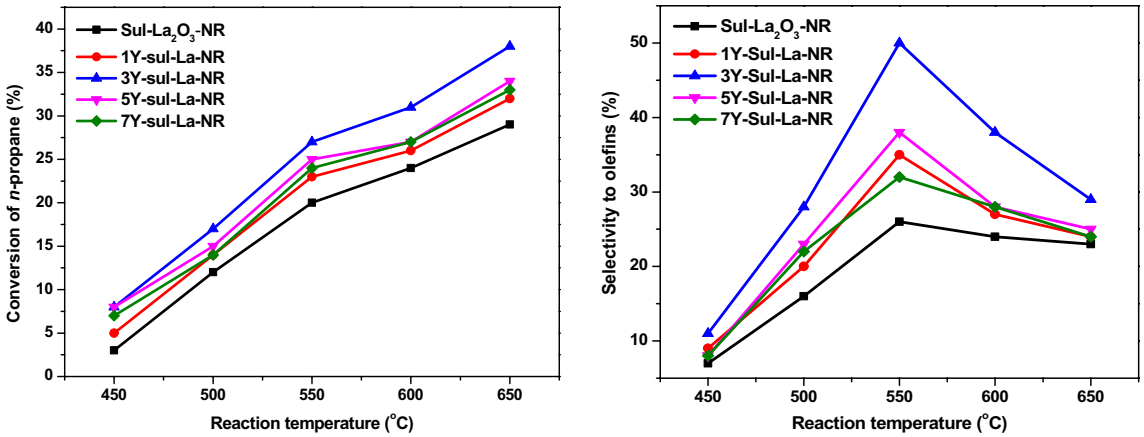

Fig. 5 Conversion of *n*-propane and selectivity to olefins at different reaction temperatures over yttrium oxide supported sulfated La_2O_3 nanorod samples

Table 3 Oxidative cracking of *n*-propane activity of yttrium oxide supported La_2O_3 and sulfated La_2O_3 nanorods at 650 °C and GHSV = 48,000 h^{-1}

Catalyst	Con. *n*-propane (%)	Selectivity of products (%)			
		Olefins	CH_4	C_2H_6	CO_x
La_2O_3-NR	23.1	22.3	3.5	7.2	67.0
Sul-La_2O_3-NR	29.2	23.2	0.7	1.5	74.6
1Y-La-NR	30.1	23.4	1.2	1.8	73.6
3Y-La-NR	35.3	27.1	1.5	2.4	69.0
5Y-La-NR	29.3	23.1	2.3	2.9	71.7
7Y-La-NR	29.2	23.3	2.4	3.2	71.1
1Y-Sul-La-NR	32.3	24.2	1.0	1.2	73.6
3Y-Sul-La-NR	38.4	29.3	2.9	2.0	65.0
5Y-Sul-La-NR	34.1	25.1	2.0	2.5	70.4
7Y-Sul-La-NR	33.2	24.1	2.3	2.8	70.8
Y_2O_3	18.3	20.3	2.7	5.0	72.0

with increase of yttrium oxide loading from 1 wt% to 3 wt% over sulfated La_2O_3-NR support. However, it was noticed that further increase of yttrium oxide loading from 3 wt% to 7 wt% resulted decrease of conversion of *n*-propane and olefins selectivity. A maximum *n*-propane conversion (38.4%) and olefins selectivity (50.3%) was observed over 3 wt% Y_2O_3 on SO_4^{2-}/La_2O_3-NR sample. It is clear that at high temperature, catalysts are producing higher amounts of undesired carbon oxides, therefore lower reaction temperatures are better to obtain high olefins selectivity. A similar behavior was observed in case of olefins selectivity patterns at studied reaction temperatures. Table 3 presents the conversion of *n*-propane and product distribution values over all the investigated catalysts at 650 °C. The catalytic activity of bare Y_2O_3 was also tested at 650 °C to compare its oxidative cracking activity with other synthesized catalysts. Bare Y_2O_3 sample offered 18.3%, conversion of *n*-propane with 20.3% olefins selectivity, which is slightly lower than bare La_2O_3-NR sample.

3.3 Stability of Yttrium Oxide Supported La_2O_3-NR Catalysts

The stability of synthesized yttrium oxide supported La_2O_3 and sulfated La_2O_3 materials in oxidative cracking of *n*-propane was studied at 650 °C. Catalytic oxidative cracking activity of 3Y-La_2O_3-NR and 3Y-Sul-La_2O_3-NR catalysts was tested for 24 h continuously, and the results were presented in Fig. 6. During the durability tests, the 3Y-La_2O_3-NR catalyst exhibited a slight decreasing trend in *n*-propane conversion and olefins selectivity levels. It is possible that aggregation of nano rods/particles of La_2O_3/Y_2O_3 could occur due to continuous operation of oxidative cracking at 550 °C and responsible for decreasing activity trend. Interestingly, the superior catalyst, 3Y-Sul-La_2O_3-NR exhibited a stable catalytic oxidative cracking activity as shown in the figure.

The results obtained from the catalyst characterization techniques could be helpful to understand the reasons for superior activity of yttrium oxide supported over sulfated La_2O_3-NR samples in oxidative cracking of *n*-propane process. The SEM image analysis indicated that all the synthesized samples possessed nano-sized tubes and particles. It is well known that nano-sized and highly dispersed metal oxides could offer a better catalytic activity than catalyst with micro-sized and agglomerated particles [38]. In recent years, morphology-dependent nanocatalysis with metal and metal oxides was reported [39]. It was observed that morphology-controlled nanomaterials with more reactive crystal planes exposed are highly efficient for different catalytic processes. In the present research the sulfated and non-sulfated

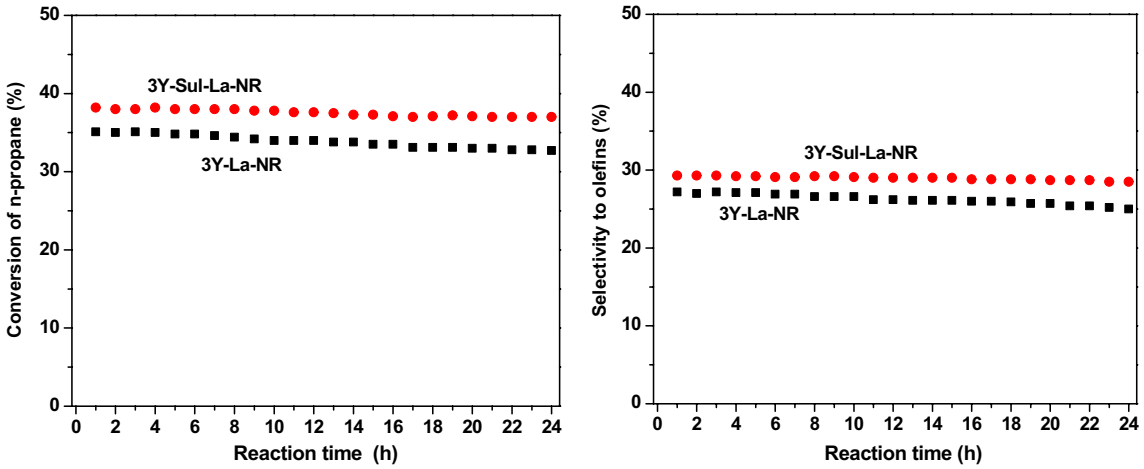

Fig. 6 Time on stream analysis of yttrium oxide supported La_2O_3-NR catalysts

catalysts exhibited same morphology (nanorods), however the sulfated samples possessed lower size compared to non-sulfated samples. It is well known that reduction of the size of particles contribute to increase the activity, so-called size-dependent catalytic chemistry. The observations from H_2-TPR experiments revealed that yttrium oxide impregnated sulfated La_2O_3 materials are easily reducible than non-sulfated La_2O_3 samples and it was also reported that the sulfated metal oxides possessed more oxygen storage capacity compared to non-sulfated metal oxides [40]. And it was also reported that presence of sulfate-metal oxide interactive species improves the mobility of lattice oxygen [41]. The SEM, N_2-physisorption, XPS, H_2-TPR and acidity measurement studies indicating that the yttrium oxide supported sulfated La_2O_3 catalysts possessed small particle size, surface area, more number of Lewis acid sites and easily reducible species; all these characteristics together assisting for the superior activity of catalysts.

4 Conclusions

Nanorods of La_2O_3 were successfully synthesized using hydrothermal synthesis method. The synthesized bulk La_2O_3 and sulfated La_2O_3 nanorods were promoted with different amounts (1, 3, 5 and 7 wt%) of yttrium oxide and utilized as catalysts for oxidative cracking of *n*-propane. Bare La_2O_3 nanorods exhibited considerable oxidative cracking activity. Enhancement in oxidative cracking activity was observed for yttrium oxide supported La_2O_3 nanorods; the highest activity was for 3 wt% yttrium oxide supported catalyst with 25% *n*-propane conversion and 36% olefins selectivity. Further improvement in catalytic activity after impregnating the yttrium oxide over sulfated La_2O_3 nanorods; around 42% *n*-propane conversion and 54% olefins selectivity was for 3 wt% yttrium oxide supported catalyst. Different techniques such as XRD, FTIR, N_2-physisorption, SEM, XPS and H_2-TPR were used to study the physico-chemical properties of samples, and the results indicated that yttrium oxide was dispersed over the La_2O_3 nanorods due to strong interaction between the two rare earth metal oxides. Deposition of yttrium oxide to the sulfated La_2O_3 nanorods resulted enhancement in the surface area and the amount of Lewis acid sites in the catalysts, which are assisting for the activation of *n*-propane. Further, the investigated catalysts exhibited stable catalytic oxidative cracking activity for 24 h without significant deactivation.

Acknowledgements The authors thank colleagues at Chemistry Department, King Abdulaziz University, Jeddah for their support.

References

1. Bender M (2014) ChemBioEng Rev 1:136
2. Louis B, Pereira M, Santos F, Esteves P, Sommer J (2010) Chem Eur J 16:573
3. Corma A, Melo FV, Sauvanaud L, Ortega F (2005) Catal Today 107–108:699
4. Xu B, Sievers C, Hong SB, Prins R, van Bokhoven JA (2006) J Catal 244:163
5. Subramanian R, Panuccio GJ, Krummenacher JJ, Leeb IC, Schmidt LD (2004) Chem Eng Sci 59:5501
6. Leveles L, Seshan K, Lercher JA, Lefferts L (2003) J Catal 218:307
7. Boyadjian CA, Lefferts L, Seshan K (2010) Appl Catal Gen A 372:167
8. Boyadjian C, Lefferts L (2018) Eur J Inorg Chem 2018:1956
9. Alonso A, Sherman AM, Wallington TJ, Everson MP, Field FR, Roth R, Kirchain RE (2012) Environ Sci Technol 46:3406
10. Sanchez-Castillo MA, Madon RJ, Dumesic JA (2005) J Phys Chem B 109:2164
11. Vogt ETC, Weckhuysen BM (2015) Chem Soc Rev 44:7342

12. Yoshimura Y, Kijima N, Hayakawa T, Murata K, Suzuki K, Mizukami F, Matano K, Konishi T, Oikawa T, Saito M, Shiojima T, Shiozawa K, Wakui K, Sawada G, Sato K, Matsuo S, Yamaoka N (2000) Catal Surv Jpn 4:157
13. Nakamura M, Takenaka S, Yamanaka I, Otsuka K (2000) Stud Surf Sci Catal 130:1781
14. Wakui K, Satoh K, Sawada G, Shiozawa K, Matano K, Suzuki K, Hayakawa T, Murata K, Yoshimura Y, Mizukami F (2002) Appl Catal A 230:195
15. Sa J, Ace M, Delgado JJ, Goguet A, Hardacre C, Morgan K (2011) ChemCatChem 3:394
16. Brown ASC, Hargreaves JSJ (1999) Green Chem 1:17
17. Venkatesh KR, Hu J, Dogan C, Tierney JW, Wender I (1995) Energy Fuels 9:888
18. Narasimharao K, Ali TT (2013) Catal Lett 143:1074
19. Al-Sultan FS, Basahel SN, Narasimharao K (2018) Fuel 233:796
20. Ding J, Wu Y, Sun W, Li Y (2006) J Rare Earths 24:440
21. Gunawidjaja R, Diez-Riega H, Eilers H (2015) Powder Technol 271:255
22. Klingenberg B, Vannice MA (1996) Chem Mater 8:2755
23. Som S, Sharma SK, Shripathi T (2013) J Fluoresc 23:439
24. Wang B, Wu X, Ran R, Si Z, Weng D (2012) J Mol Catal A 361–362:98
25. Xu JQ, Xiong SJ, Wu XL, Li TH, Shen JC, Chu PK (2013) J Appl Phys 114:093512
26. Sunding MF, Hadidi K, Diplas S, Løvvik OM, Norby TE, Gunaes AE (2011) J Electron Spectrosc Relat Phenom 184:399
27. Dallera C, Giarda K, Ghiringhelli G, Tagliaferri A, Braicovich L, Brookes NB (2001) Phys Rev 64:153104
28. Moulder JF, Stickle WF, Sobol PW, Bomben KD (1992) Handbook of x-ray photoelectron spectroscopy. Perkin-Elmer, Eden Prairie
29. Smirnov MY, Kalinkin AV, Pashis AV, Sorokin AM, Noskov AS, Kharas KC, Bukhtiyarov VI (2005) J Phys Chem B 109:11712
30. Tresintsi S, Simeonidis K, Pliatsikas N, Vourlias G, Patsalas P, Mitrakas M (2014) J Solid State Chem 213:145
31. Stypula B, Stoch J (1994) Corros Sci 36:2159
32. Baltrusaitis J, Cwiertny DM, Grassian VH (2007) Phys Chem Chem Phys 9:5542
33. Howng WY, Thorn RJ (1980) J Phys Chem Solids 41:75
34. Stoychev D, Valov I, Stefanov P, Atanasova G, Stoycheva M, Marinova T (2003) Mater Sci Eng, C 23:123
35. Sasikala R, Varma S, Gupta NM, Kulshreshtha SK (2001) J Mater Sci Lett 20:1131
36. Au CT, Zhou TJ, Lai WJ, Ng CF (1997) Catal Lett 49:53
37. Lange J-P, Gutsze A, Karge HG (1988) J Catal 114:136
38. Akay G (2016) Catalysts 6:80
39. Umar A, Kumar R, Akhtar MS, Kumar G, Kim SH (2015) J Colloid Interface Sci 454:61
40. Bazin P, Saur O, Marie O, Daturi M, Lavalley JC, Le Govic AM (2012) Appl Catal B 119–120:207
41. Si Z, Weng D, Wu X, Ma Z, Ma J, Ran R (2013) Catal Today 201:122